A NEW APPROACH FOR SIMULATION OF HOT MIX ASPHALT; NUMERICAL AND EXPERIMENTAL

M. Vadood* **M. S. Johari**

Textile Engineering Department
Amirkabir University of Technology
Tehran, Iran

A. R. Rahai

Civil and Environmental Engineering Department
Amirkabir University of Technology
Tehran, Iran

ABSTRACT

In this study a novel approach for 3D modeling of cylindrical sample of hot mix asphalt (HMA) is presented. To this end, the cylindrical sample was divided into several slices and using a developed algorithm the processed images were extended to 3D volumetric objects to reconstruct the 3D microstructure of HMA. To evaluate the efficiency of the presented 3D model for prediction of mechanical behavior, HMA was regarded as a two-phase mixture; mastic phase and aggregate phase. The asphalt binder, filler, air voids and fine aggregates were considered as mastic with viscoelastic behavior and the aggregate was considered as an elastic material. Two models (Burger and generalized Kelvin) were studied for determining viscoelastic behavior of mastic. Finally, to verify the model using Finite Element Method (FEM) the behavior of the 3D model was simulated under different uniaxial compressive loads. A good agreement was observed between the simulated results and corresponding experimental data which indicates the efficiency of the proposed model to simulate three-dimensional asphalt.

Keywords: Hot mix asphalt, Image processing, 3D modeling, Microstructure.

1. INTRODUCTION

Hot mix asphalt (HMA) is composed of coarse and fine aggregates, bitumen, air voids, and filler and in some cases additive such as high tenacity fibers, brimstone and rubber. Many studies have focused on the relation between the macroscopic response of HMA and its components properties (*e.g.* Airey *et al*. [1]). One of the most important components of HMA is aggregate and its structural characteristics which determine the mechanical behavior of the HMA. On the other hand, the collection of bitumen, filler and air voids is a matrix which contains aggregates. Therefore the properties of this collection such as stiffness, viscosity, and cohesion can directly influence the behavior of HMA. At the present time, various laboratory tests exist to evaluate the mechanical and physical performance of HMA. Most of these techniques are time-consuming, tedious and expensive. As an alternative approach, the micro simulation of HMA and evaluating its behavior using numerical methods have been established. Recently, some researchers have presented two-dimensional models to simulate mechanical behavior of HMA. Sadd *et al.* [2] modeled asphalt concrete to simulate the indirect tension test by assuming that the aggregates are two-dimensional ellipses of different diameters and orientations. A series of simulations were performed and their results were compared with those obtained through experimental tests. In related studies, Sadd and Dai [3] and Dai and You [4] used the same modeling approach to simulate the behavior of cemented particulate materials and predict the creep stiffness of asphalt mixture using Finite Element Method (FEM). Bandyopadhyaya *et al.* [5] and Mitra *et al.* [6] used the cross-section images of HMA to simulate the behavior of HMA subjected to a line load at constant displacement rate and study the response. The best-fitted ellipse for each grain in cross-section images was considered. The ellipses then were distributed under random orientation in cross-section region and the overlap criteria of these ellipses were checked using the algorithm proposed by Džiugys and Peters [7]. The numerical results were compared with experimental measurements and observed to match well with experimental results. Wang and Hao [8] and Dai [9] used original cross-section images of HMA sample to simulate the indirect tensile test under various conditions and predict the dynamic modulus and phase angle of asphalt. Some researchers used nondestructive X-ray micro-computed tomography (XCT) for modeling HMA. Masad *et al.* [10] and Gatchalian *et al.* [11] captured the internal structure image of HMA using X-ray CT to study air void distribution and aggregate resistance to degradation in asphalt mixtures, respectively. The lattice model has also been used by some researchers to simulate the mechanical properties of materials with complex microstructures such as HMA. Schlangen and Garboczi [12] applied the lattice model

* Corresponding author (mortezavadood@gmail.com)

DOI : 10.1017/jmech.2015.36
Copyright © 2015 The Society of Theoretical and Applied Mechanics, R.O.C.
https://doi.org/10.1017/jmech.2015.36 Published online by Cambridge University Press

to simulate crack propagation and analyze its failure mechanism. Ince *et al.* [13] developed the lattice model to simulate load-deformation of notched three point bending beams of various sizes. Yang *et al.* [14] applied this model to simulate macro-response of asphalt mixture under uniaxial compression and the effect of aggregate proportion on the HMA elastic modulus was studied. Despite of wide applications, the lattice model only considers aggregate content and random aggregate distributions. Bazant *et al.* [15] used the random particle model to simulate the particle solid material supposing the aggregates are made of the random distributed circular particles of fixed shape. Similarly, Fu and Dekelbab [16] presented a 3D simulation method based on the random particle model through both the kinematics and dynamic analysis. The other method called arbitrary polyhedron model assumes that the mechanical properties of HMA are based on the aggregates shapes, angularity, size and gradation. To simulate the aggregate, a random polygon or polyhedron function is used and the extension operation is controlled using the convexity criteria. Du and Sun [17] presented a two-dimensional simulation of aggregate with arbitrary shapes, in which all aggregates were generated at one time and then the arbitrary shaped aggregates were created by random extension. Yin *et al.* [18] presented a heterogeneous fracture modeling technology to simulate complex two-dimensional crack propagation in asphalt mixture. Moreover, Yin *et al.* [19,20] and Zeng *et al.* [21] used a two-dimensional modeling frame in basis of the aggregate generation and packing algorithm. This frame was used to study the effects of aggregate distribution and crack location, initiation and propagation behaviors in pre-cracked three-point bending asphalt mixture beam.

3D models are more realistic than 2D ones and consequently their results are more reliable. However, because of very high computational cost and complexity in 3D microstructure modeling of HMA, most of the presented models are 2D based. In recent years, some 3D microstructural modeling of HMA has been presented. Collop *et al.* [22] and Mo *et al.* [23] by using spheres to represent the aggregates simulated the microstructure of asphalt mixture highly idealized. Xu *et al.* [24] presented a method for 3D simulating of HMA. In their method using arbitrary polyhedron algorithm, the aggregates are generated and randomly packed in a given cylindrical or cubical region one by one of equal probably. Yang *et al.* [25] developed a 3D random modeling frame capable to efficiently establish numerical asphalt mixture samples involving the graded polyhedric coarse aggregates. This frame was successfully applied to fracture modeling and analyses of the asphalt mixture samples subjected to uniaxial tension. Shashidhar and Gopalakrishnan [26] studied the aggregate structure in HMA using internal images scanned by X-ray CT to prepare digital models in 3D. In this method, many X-ray images were prepared from different cross-sections of sample and by combination of all images the sample structure was reconstructed as it is. Coleri *et al.* [27] and You *et al.* [28] simulated the internal microstructure of HMA using X-ray CT to predict shear modulus at high temperatures with a range of loading frequencies.

There is a considerable gap between the actual microstructure of HMA and the real case in 2D modeling. Therefore, the present study aims to introduce a new, inexpensive and easy-to-use approach for 3D simulation of HMA based on the scanned cross-section images. To evaluate the efficiency of the presented model in prediction of mechanical behavior, HMA was considered as a two-phase material; mastic (viscoelastic) phase and aggregate (elastic) phase. Two models were studied for determining viscoelastic behavior of mastic. Finally, the behavior of the 3D model was simulated under different uniaxial compressive loads using the FEM and the results were compared with those obtained through experimental tests.

2. MATERIAL AND METHODOLOGY

Due to simplicity of sample preparation, Marshall samples were selected for experimental analysis. Four samples were prepared based on the Marshall method (Asphalt Institute, MS-2) with a 12.5mm nominal maximum aggregate size, 60/70 penetration grade bitumen and cement powder as filler. Figure 1 shows the aggregate gradation. The asphalt-aggregate ratio was 95% of the weight of mixture and void ratio was $4 \sim 5\%$ for all prepared samples.

To simulate the internal structure of cylindrical sample of HMA, one of the samples was cut horizontally into thin slices using a diamond blade as shown in Fig. 2. In the cutting procedure, one end of sample was fixed by clamps while the other end was free. Since the slice thickness below 12mm changes during the cutting process, thinner slices were not possible to be prepared. Due to this technical limitation, the height of made samples was 70mm which slightly is different from the typical Marshall sample. The made sample, however, in this study is called Marshall sample. Moreover, a thin layer with thickness of approximately 1mm was removed from the top and bottom of the sample.

Afterwards, the side of each cutting plane with lower inner broken aggregates was chosen and scanned via Hp-Scanner 2420 of 600dpi resolution. Using this imaging technique not only is simple, but also the aggregates in the scanned image are the same as they look in the cutting plane. Figure 3 depicts an image of a cutting plane in which the darker area is the binder surrounded the aggregates.

Using the above procedure, four images from the cutting planes and two images from the top and bottom of sample were obtained.

2.1 Segmentation

The distance transform is a technique which measures the minimum distance between each pixel belonging to an object and the background by pixel by pixel scanning of the entire image [29]. As a result,

https://doi.org/10.1017/jmech.2015.36 Published online by Cambridge University Press

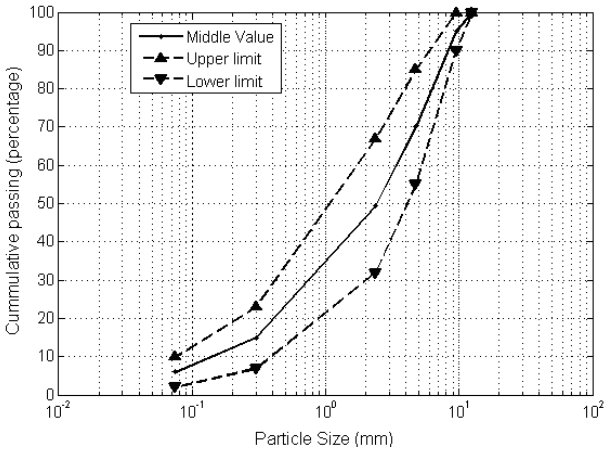


Fig. 1 Aggregate gradation used in prepared samples.

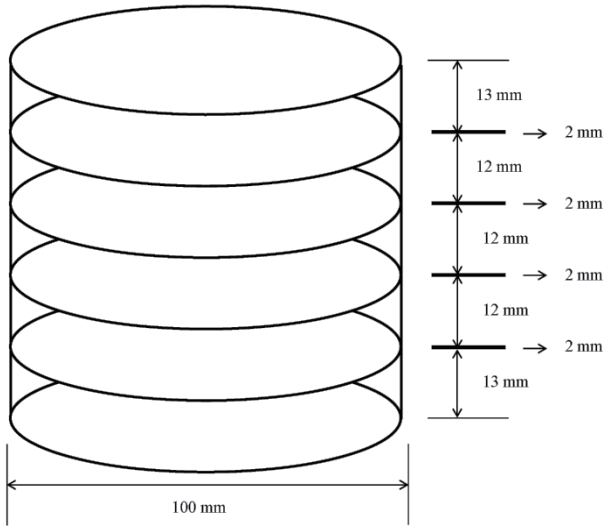


Fig. 2 The horizontal positions of cutting planes on the cylindrical samples, the thickness of the diamond blade is 2mm.



Fig. 3 The prepared image of the cross-section in cutting plane.

the pixels closer to the center of object obtain higher values. The watershed transform is generally applied on the output of the distance transform to segment joined objects in 2D or 3D spaces. In this technique, the pixels of the transformed object are integer values greater than or equal to 0. Actually the pixels having the value of 0 are the boundaries between the joined aggregates [30]. Figure 4 indicates an example of separation of two joined circles using distance and watershed transforms.

To separate the aggregates and their boundaries from binder, the image processing technique proposed by the recent work of Vadood *et al.* [30] was applied. By converting images format into l*a*b* color space system and selecting appropriate threshold value (0.01), the boundaries of aggregate can be traced out. Due to the high closeness of some adjacent aggregates, they may be detected as one aggregate. It is necessary to detect these aggregates and remove their overlap before any further analysis. To this end, these aggregates were separated using distance and watershed transforms. Figure 5 shows the output image of cross-section after segmentation process.

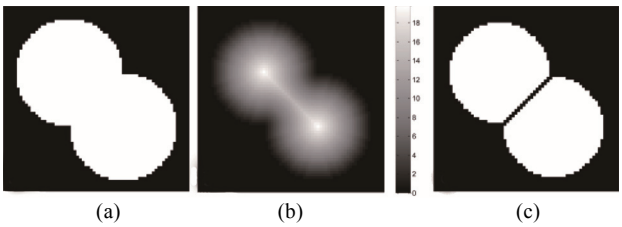


Fig. 4 (a) two joined circles, (b) the image of distance transform for Fig. 4(a), (c) the output of applying the watershed transform on the image in Fig. 4(b).

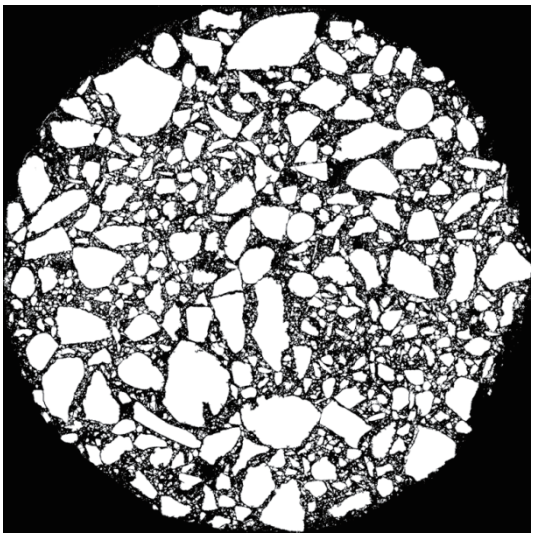


Fig. 5 The cross section image shown in Fig. 3 after applying segmentation process.

https://doi.org/10.1017/jmech.2015.36 Published online by Cambridge University Press

2.2 Geometric Characteristics

Knowing that not all aggregates are round, there are many elliptical descriptors to describe the shape of aggregate. The second moment of a best-fitted ellipse to an aggregate shape is one of them which is easy to understand and use. As already mentioned, some researchers replaced aggregates by the best-fitted ellipses in two-dimensional image. In Fig. 6, a grain with an arbitrary shape and its best-fitted ellipse are shown. The orientation angle between the major axis of the best-fitted ellipse and x axis is θ.

After segmentation operation, a set of geometric properties of aggregates in the image is measured. The following quantities of each aggregate are determined:

- Major axis of the ellipse: A scalar value which is the length of the major axis of the ellipse surrounding the aggregate in pixels, having the same normalized second central moments as the object.
- Minor axis of the ellipse: A scalar value which is the length of the minor axis of the ellipse surrounding the aggregate in pixels, having the same normalized second central moments as the object.
- Center: The coordinate of center of mass of the object in the image.
- Orientation: The angle between the x-axis and the major axis of the ellipse that has the same second-moments as the region.

3. 3D MODELING

In this study, it was assumed that the cylindrical sample of HMA is composed of two phases, including aggregate and mastic asphalt. Due to the large number of fine aggregates in the cross-section images, the computational cost increases extremely and makes the process unnecessarily complicated. To avoid this problem and to simplify the computations, generally the binder, filler, air voids and fine aggregates are considered as mastic asphalt bonded perfectly to the aggregate phase [5,8,28]. In this study, the binder, filler, air voids and fine aggregates smaller or equal to 2.36mm were considered as mastic asphalt. For 3D simulation, each aggregate is converted to the 3D volumetric object. As already mentioned, some researchers assumed that each aggregate can be replaced in the cross-section image by its best-fitted ellipse [5]. This assumption can be extended in 3D modeling. To this end, at the first step, each aggregate in two-dimensional images which is larger than 2.36mm is replaced by its best-fitted ellipse. Afterwards, each ellipse is rotated along its own major diameter through 180 degrees. Using this method, the aggregate is replaced by the elliptical sphere. Figure 7(a) depicts an aggregate which its major diameter is along Z axis. Using this technique the aggregate has been replaced by an ellipse on the ZY plane. Rotating the ellipse along its major diameter generates an elliptical sphere along Z axis. In fact, this sphere is made of parallel cross-sections to the XY plane at various heights of Z as illustrated in Fig. 7(b). The red and blue areas show the cross-sections of elliptical sphere parallel to the XY plane and free space, respectively.

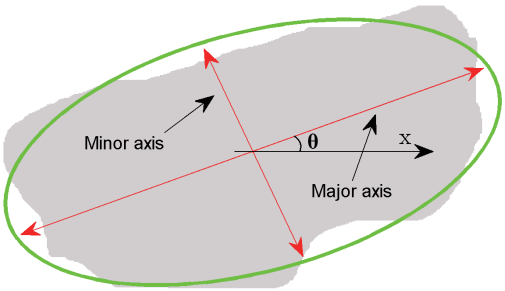
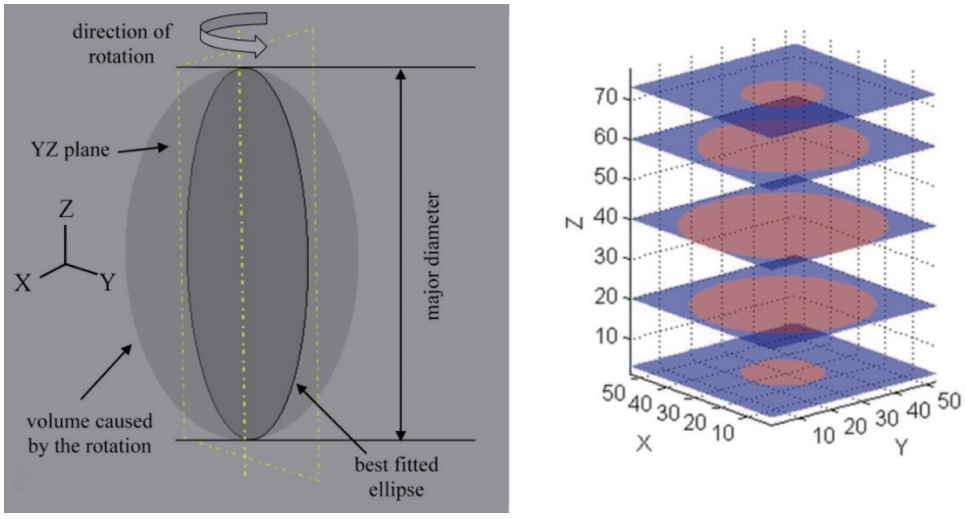


Fig. 6 A grain with an arbitrary shape together with the best-fitted ellipse.



(a) (b)

Fig. 7 (a) rotation of the best fitted-ellipse along its major diameter, (b) the cross-sections of the elliptical sphere parallel to the XY plane in various heights.

https://doi.org/10.1017/jmech.2015.36 Published online by Cambridge University Press

Since the negative coordinates do not exist in the 3D volumetric objects, the lowest coordinates of the elliptical spheres on the Z axis is shifted to height 0. As a matter of fact, each cross-section is a two-dimensional image and merging these cross-sections generates the 3D volumetric object corresponding to the assumed aggregate.

When all aggregates in the cutting plane are replaced by elliptical spheres, some of adjacent spheres slightly overlap. To remove overlaps a further segmentation process is needed. Figure 8(a) demonstrates two adjacent elliptical spheres with a slight overlap. By applying the distance and watershed transforms over all the cross-sections parallel to XY plane, the overlap areas can be detected and subsequently removed. Figure 8(b) depicts a schematic of two modified cross-sections which by merging these cross-sections two separated 3D objects are obtained as shown in Fig. 8(c).

By replacing all aggregates in the cross-section image with elliptical spheres and controlling overlaps using distance and watershed transforms, a 3D volumetric layer will be obtained, while the cross-section image is in the symmetric plane. With the exception of top and bottom of sample, the generated 3D layer for all cutting plane images is generated completely. For the images taken from the top and bottom, the lower and top half are considered, respectively. Figure 9 illustrates the procedure to create 3D volumetric layers for cylindrical HMA sample.

Merging all the 3D constructed layers presents aggregates in the cylindrical sample of HMA (Fig. 10(a)).

If all the 3D layers are removed from 3D cylindrical volume with the diameter and height of a Marshall sample, the remained volume would be the mastic asphalt (Fig. 10(b)). By combining two parts shown in Fig. 10, the HMA sample is reconstructed in 3D. To evaluate the efficiency of the presented approach for prediction the mechanical behavior, the 3D model was imported into the FEM software.

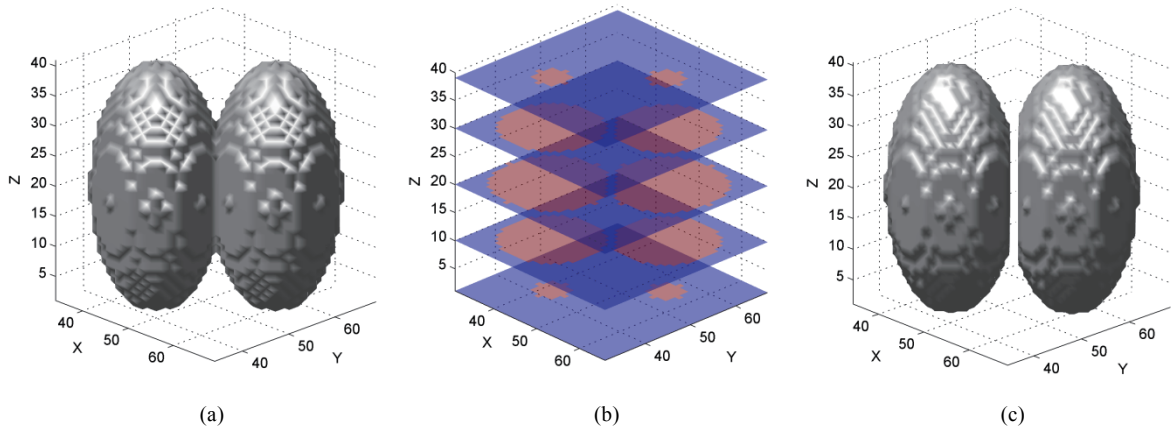
To use FEM, it is necessary that all parts of the model to be meshed. Due to the removing of overlaps, some objects have complex shapes. Hence, the 4-node linear tetrahedral element (1 integration point) with three degrees of freedom for each node was considered to mesh. A Matlab program was developed to generate mesh [31]. As the size of volumetric objects is not the same (Fig. 10(a)), using global mesh size for all objects leads to a significant increase in the calculation cost. It was found that the size of volumetric objects could be divided into 5 classes and therefore each object was meshed regarding to its class (0.5, 0.55, 0.65, 0.7 and 0.75mm as mesh size for very fine, fine, medium, coarse and very coarse classes). Figure 11 depicts a meshed 3D object using very fine and very coarse meshes. As can be observed, the number of elements for very coarse mesh reduces approximately up to 18% in comparison with that of very fine mesh.

Therefore, the fine and coarse aggregates get fine and coarse mesh, respectively. Finally 554,237 tetrahedral elements were generated for all the 3D objects presenting aggregates. 3D volumetric mastic asphalt was meshed and contained 1,883,595 tetrahedral elements by mesh size of 0.85 mm. A part of mastic asphalt together with 3D objects is shown in Fig. 12. The number of elements is large enough to obtain a converged FEM solution, indicating the increase in the number of elements just rises the computation time and provides no significant improvement in the obtained results.

The combination of the meshed mastic asphalt and 3D objects as aggregates makes a virtual Marshall sample which can be imported into the Finite Element software.

4. MATERIAL PROPERTIES

Determining the mechanical properties of material is of great importance in numerical simulations such as FEM. By keeping the proportions of mastic components for the Marshall sample, mastic sample of 70mm height and 100mm diameter was prepared exactly in the same way as Marshall samples were prepared. The mastic sample was placed in a chamber with 25°C for 24 hours and then the static creep test was conducted on the mastic sample at 25°C. The mastic asphalt can be considered as linear viscoelastic material at small



(a) (b) (c)

Fig. 8 (a) two adjacent elliptical spheres, (b) modified cross-sections parallel to the XY plane, (c) merged cross-sections.

https://doi.org/10.1017/jmech.2015.36 Published online by Cambridge University Press

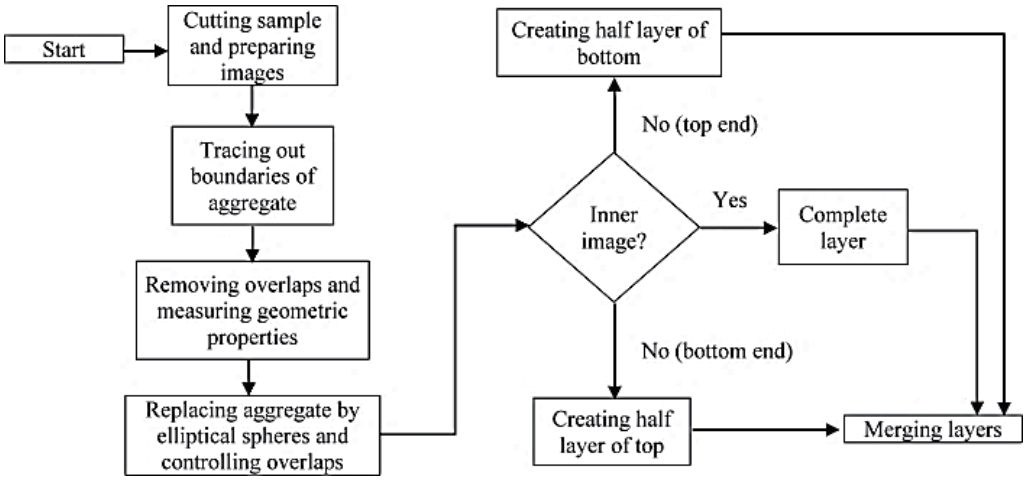
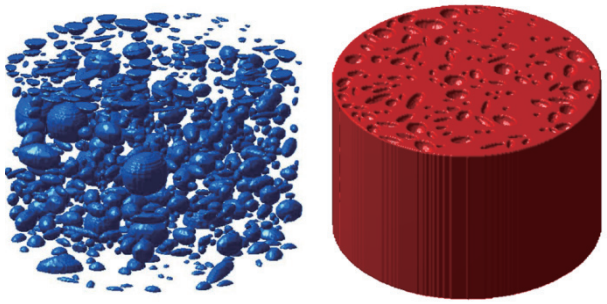
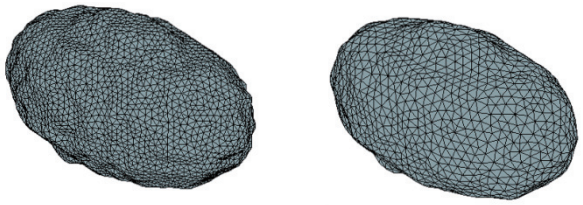


Fig. 9 The procedure to create 3D volumetric objects for replacing the aggregates.



(a) (b)

Fig. 10 (a) all 3D objects presenting aggregates in HMA structure, (b) extracting Fig. 9(a) from a cylindrical volume with the size of Marshall sample (mastic phase).



(a) (b)

Fig. 11 (a) very fine mesh: 40969 elements, (b) very coarse mesh: 33,484 elements.

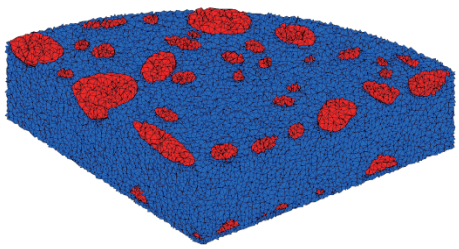


Fig. 12 A part of cylindrical sample of HMA, 3D objects which present aggregates: Red area, mastic asphalt: Blue area.

strains [32]. It was found that the strain in the creep test was 0.8%, so the linear viscoelastic behavior was considered for the mastic phase. The sample was placed from top and bottom between two steel plates. The lower plate was fixed and a compressive load (600KPa) was applied on the top plate for 3,400s. Generally the Burger model (Maxwell (m) and Kelvin (*k*) spring-dashpot in series) is applied to describe the linear viscoelastic behavior based on Eq. (1).

$$D(t)=\frac{1}{E_m}\left(1+\frac{tE}{\eta_m}\right)+\frac{1}{E_m}\left(1-e^{\frac{-t.E_k}{\eta_k}}\right) \tag{1}$$

whereas D, t, E and η are the creep compliance, time, elastic modulus and viscoelastic coefficient, respectively. Furthermore, the creep compliance for solids can be easily characterized using generalized Kelvin model in series (Prony series) based on Eq. (2). The ability of Prony series to capture the behavior of viscoelastic materials is related to their series type of structure. Hence depending on the complexity of material behavior, the number of Kelvin units can be adjusted.

$$D(t)=D_g+\sum_{j=1}^{n}D_j\left(1-e^{\frac{-t}{\tau_j}}\right) \tag{2}$$

whereas D_g denotes the glassy compliance and D_j and τ_j are the retardation strength and time of j^{th} Kelvin unit, respectively. A Matlab program was developed to fit a curve based on the Eqs. (1) and (2) on the experimental creep data. Figure 13 shows the experimental creep data, fitted Burger model and Prony series for the mastic sample. Table 1 indicates the computed parameters for Burger model and Prony series.

According to Fig. 13 and Table 1, Prony series with more than three Kelvin units satisfactorily captured the trend of experimental creep data which proves that Prony series can indicate the behavior of mastic asphalt at small strains. In this study, Prony series with $j = 5$

https://doi.org/10.1017/jmech.2015.36 Published online by Cambridge University Press

Table 1 The computed parameters for Burger model and Prony series (j = 2 to 5).

Prony Series		D_i	τ_i	D_g (MPa^{-1})	SSE*
The number of Kelvin units (j)	5	0.00180	0.64864	1.66E−07	1.16E−06
		0.00174	4.76427		
		0.00213	15.72482		
		0.00261	109.21361		
		0.00408	1241.75175		
	4	0.00165	0.99992	2.25E−04	2.67E−06
		0.00311	7.39796		
		0.00290	68.83161		
		0.00424	988.27540		
	3	0.00069	0.38843	2.43E−04	4.96E−05
		0.00592	10.00000		
		0.00490	599.68741		
	2	0.00614	10.00000	7.30E−04	5.04E−05
		0.00489	609.37149		
Burger model SSE=2.053E−4		E_m (MPa)	η_m (MPa)	E_k (MPa)	η_k (MPa)
		4.13E+02	6.74E+05	1.63E+02	7.14E+03

*Sum of Square Error

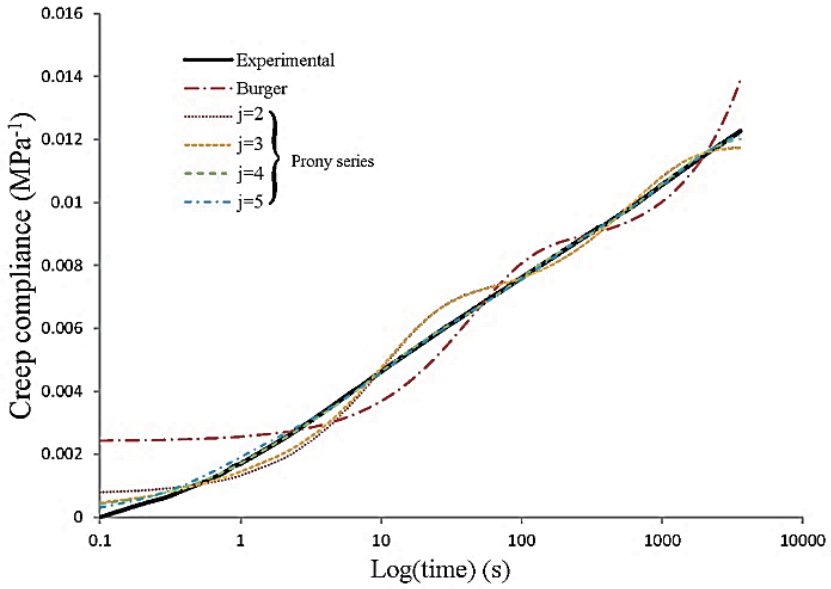


Fig. 13 The experimental creep compliance data, fitted Burger model and Prony series (j = 2 to 5).

was selected to model the mastic properties (Table 1). Generally, the properties of viscoelastic material are expressed by relaxation modulus as presented in Eq. (3).

$$E(t) = E_e + \sum_{i=1}^{m} E_i e^{\frac{-t}{\rho_i}} \tag{3}$$

where E denotes the relaxation modulus, E_e is the stability modulus, and E_i and ρ_i are the material coefficients. The creep compliance and relaxation modulus are related to each other by a convolution integral (Eq. (4)):

$$\int_0^t D(t-\tau)\frac{dE(\tau)}{d\tau}d\tau = 1 \quad (t>0) \tag{4}$$

where τ is an integration variable. Substituting Eqs. (2) and (3) in Eq. (4) and solving the obtained equation leads to linear algebraic Eq. (5). Therefore, if the set of $D(t)$ (D_g, D_j and τ_j) is known, the set of $E(t)$ (E_e, E_i and ρ_i) can be calculated.

$$A_{ki}E_i = B_k \tag{5}$$

where

https://doi.org/10.1017/jmech.2015.36 Published online by Cambridge University Press

$$A_{ki}=\begin{cases}-D_g\left(1-e^{\frac{-t_k}{\rho_i}}\right)-\sum_{j=1}^{n}D_j(1-e^{\frac{-t_k}{\rho_i}}) \\ \qquad +\sum_{j=1}^{n}\frac{D_j\tau_j}{\tau_j-\rho_i}\left(e^{\frac{-t_k}{\tau_j}}-e^{\frac{-t_k}{\rho_i}}\right) & [\rho_i\neq\tau_j] \\ -D_g\left(1-e^{\frac{-t_k}{\rho_i}}\right)-\sum_{j=1}^{n}D_j(1-e^{\frac{-t_k}{\rho_i}}) \\ \qquad +\sum_{j=1}^{n}\frac{D_j t_k}{\rho_i}e^{\frac{-t_k}{\tau_j}} & [\rho_i=\tau_j]\end{cases} \tag{6}$$

$$B_k=1-\frac{D_g+\sum_{j=1}^{n}D_j\left(1-e^{\frac{-t_k}{\tau_j}}\right)}{E_e} \tag{7}$$

$$E_e\equiv\lim_{t\to 0}E(t)=\frac{1}{D_g+\sum_{j=1}^{n}D_j} \tag{8}$$

where t_k (k = 1, …, p) indicates a discrete time corresponding to the upper limit of integration in Eq. (4). To define the ρ_i coefficients, the graphical method introduced by Park and Schapery [33] was used. Using this method results in slight error (below 4%) due to the numerical error and can be ignored. Figure 14 shows the absolute value of the Laplacian compliance as a function of the negative inverse of the Laplacian time. In this way, the corresponding x value (horizontal axes) of local minimum is an approximation of the unknown ρ_i constant.

At this time, Eq. (5) can be solved for obtaining the unknown E_i using known parameters D_i, τ_i and ρ_i. Table 2 shows the relaxation modulus parameters for Prony series with j = 5 based on Eq. (3).

The behavior of a linear isotropic viscoelastic material can be formulated in the FEM software (Abaqus) with deviatoric stress-strain relations as Eqs. (9) to (11) [25].

$$S_{ij}=\int_0^t 2G(t-\tau)\frac{de_{ij}(\tau)}{d\tau}d\tau \tag{9}$$

$$G(t)=1-\sum_{i=1}^{N}g_i^P(1-e^{-t/\alpha_i^G}) \tag{10}$$

$$G=\frac{E}{2(1+\upsilon)} \tag{11}$$

where S_{ij} and e_{ij} are deviatoric stress and strain respectively, G denotes shear relaxation modulus, υ is Poisson's ratio and N, g_i^P and α_i^G (i = 1,…,N) are material constants. According to Table 2 and using Eqs. (3) and (11), shear relaxation modulus data can be determined. In the next step, a curve based on Eq. (10) was fitted on the normalized shear relaxation modulus data with high accuracy (correlation coefficient = 0.99) and the material constants were obtained for using in the FEM software (Table 3).

For the mastic asphalt, E_e was used as the instantaneous elastic modulus and different values (0.30, 0.35 and 0.40) were considered as Poisson's ratio at temperature of 25°C [5,24,34]. It was observed Poisson's ratio of 0.35 obtains the best results. Also, the aggregate was defined as an elastic material having 50GPa and 0.25 elastic modulus and Poisson's ratio, respectively [8]. The stress-strain equation for elastic material behavior is shown as Eq. (12) [32].

$$\begin{aligned}\sigma_x&=E\varepsilon_x\\ \varepsilon_y&=-\upsilon\frac{\sigma_x}{E}\\ \varepsilon_z&=-\upsilon\frac{\sigma_z}{E}\end{aligned} \tag{12}$$

where σ and ε are stress and strain respectively, and x, y and z subscripts denote the X, Y and Z direction in cartesian coordinates.

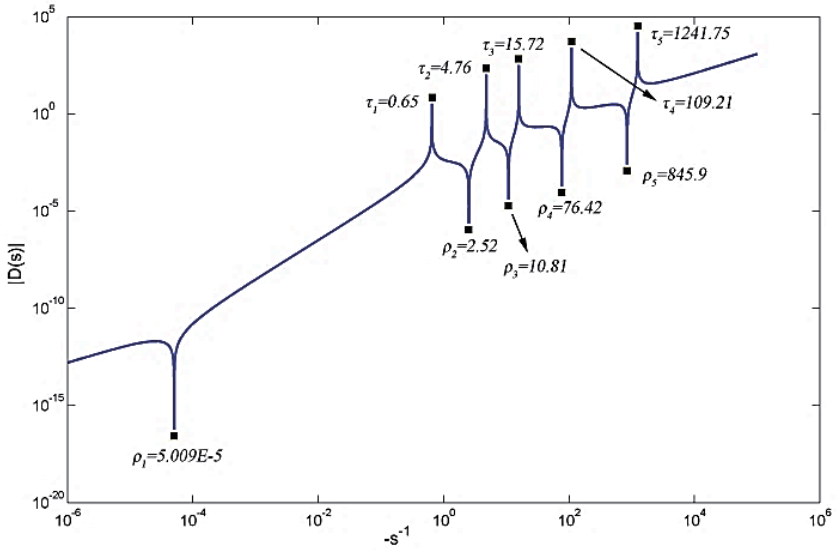


Fig. 14 The absolute value of the Laplacian compliance | D(s) | versus the negative inverse of the Laplacian time ($-S^{-1}$) for Prony series (Table 2, degree of freedom: 5).

https://doi.org/10.1017/jmech.2015.36 Published online by Cambridge University Press

Table 2 The relaxation modulus parameters for Prony series ($j = 5$) based on Eq. (3).

i	E_i	ρ_i
1	–745.34444	0.00005
2	841.82938	2.52000
3	–225.54778	10.81000
4	100.58056	76.42000
5	28.35576	845.90000
E_e	80 MPa	

Table 3 The material constants in Eq. (10) for using in the FEM software.

i	g_i^p	α_i^G
1	0.79148	2.03504
2	1.14E–10	10
3	0.07843	127.24
4	0.03067	1200
5	4.32E–14	173829

5. SIMULATION OF CREEP BEHAVIOR

Once the aggregates and mastic asphalt were modeled as 3D objects and their properties were defined, the presented approach should be validated. One of the most important mechanical behaviors of HMA is its static creep behavior. The deformation of virtual Marshall sample under three compressive uniaxial loads 100, 300 and 500KPa was simulated using Abaqus/Standard solver. The simulation was conducted on a system with 16 processors and 32GB of memory. The results were compared with the corresponding experimental data for 3600 seconds. Two discrete rigid plates were considered at the top and bottom of the 3D simulated Marshall sample. The bottom plate was set to be an encastre constraint and the uniformly distributed load was exerted on the top plate which was free to move only in loading direction. With the intention of applying load similar to actual test, it was assumed that the rigid plates are completely in contact with the sample and no slippage occurs. A surface to surface contact constraint was used between the rigid plates and the sample. Furthermore, it should be mentioned that the objects as aggregates and mastic part were in tie constraint. The displacement of the central point for the top plate in experiment and simulation was considered as a function of time loading and is shown in Fig. 15. For real creep test the specimens were placed in the chamber with 25°C for 24 hours. As can be seen, the experimental curve and FEM output for each case of loading are very similar and show the same trend. This indicates that the introduced method is reliable and can be applied for 3D modeling of HMA as a two-phased material. It is worthy of mention that the presented method can be applied for other shape of HMA samples.

As can be seen, there is better agreement between the experimental and FEM output at lower stress level, however their gap obviously increases with increasing stress level. The possible reason is that the generalized Kelvin model cannot perfectly describe the nonlinear creep behavior of asphalt mastic. Because of using diamond blade, the cylindrical sample was divided into five slices. This causes loss of some aggregates between the two cutting planes. Obviously dividing the cylindrical samples into more slices results in more realistic model and hence the model performance would be much closer to the experimental results. The contact surfaces between aggregates have a great effect on the mechanical behavior of HMA, especially at higher loading levels. In this study it was assumed that the aggregates can be replaced by elliptical spheres. This assumption satisfactorily works at lower loading levels. At higher loadings due to the fact that the surface of elliptical spheres cannot simulate the real contact between aggregates, the FEM prediction is not as accurate as the case for lower loadings. Moreover, to simplify the model, air voids were considered as a part of mastic asphalt. It is worthy of mentioning that considering air voids as a separated phase leads to higher accuracy in modeling.

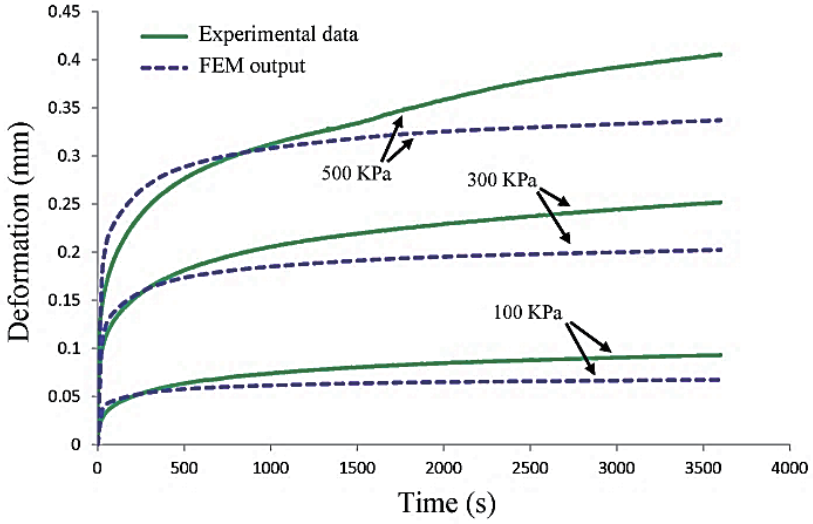


Fig. 15 Creep behavior under different uniaxial compressive loads; numerical and experimental.

https://doi.org/10.1017/jmech.2015.36 Published online by Cambridge University Press

6. CONCLUSIONS

In this paper a novel method was introduced for 3D modeling of HMA microstructure using image processing techniques. After dividing the HMA sample into several slices, the images of cross-sections were captured and processed using a developed algorithm to separate aggregate from binder. Afterwards, the 3D microstructure of the asphalt mixture was obtained by using a number of parallel 2D images. The HMA sample was considered as a two-phased material; aggregate phase (*i.e.* aggregates larger than 2.36mm) and mastic phase (*i.e.* asphalt binder, filler, air voids and aggregates smaller or equal to 2.36mm). The aggregates were considered elastic while the mastic asphalt was assumed linear viscoelastic the behavior of which was described using two models. Prony series based on the generalized Kelvin model showed an excellent fit on the experimental creep compliance data. To verify the presented model, the deformation of HMA sample under different compressive uniaxial loadings was simulated and compared with the corresponding experimental results. A very good agreement between the FEM and experimental results was obtained, especially for lower loading levels. The introduced method enjoys the advantage of easy and inexpensive 3D modeling of HMA, without needing special equipment such as X-ray tomography.

ACKNOWLEDGEMENTS

The authors greatly appreciate the help given by Dr. Hamid Reza Sanjari during the course of research.

REFERENCES

1. Airey, G., Collop, A., Zoorob, S. and Elliott, R., "The Influence of Aggregate, Filler and Bitumen on Asphalt Mixture Moisture Damage," *Construction and Building Materials*, **22**, pp. 2015–2024 (2008).
2. Sadd, M. H., Dai, Q., Parameswaran, V. and Shukla, A., "Simulation of Asphalt Materials Using Finite Element Micromechanical Model with Damage Mechanics," *Transportation Research Record: Journal of the Transportation Research Board*, **1832**, pp. 86–95 (2003).
3. Sadd, M. H. and Dai, Q., "A Comparison of Micro-Mechanical Modeling of Asphalt Materials Using Finite Elements and Doublet Mechanics," *Mechanics of Materials*, **37**, pp. 641–662 (2005).
4. Dai, Q. and You, Z., "Prediction of Creep Stiffness of Asphalt Mixture with Micromechanical Finite-Element and Discrete-Element Models," *Journal of Engineering Mechanics*, **133**, pp. 163–173 (2007).
5. Bandyopadhyaya, R., Das, A. and Basu, S., "Numerical Simulation of Mechanical Behaviour of Asphalt Mix," *Construction and Building Materials*, **22**, pp. 1051–1058 (2008).
6. Mitra, K., Das, A. and Basu, S., "Mechanical Behavior of Asphalt Mix: An Experimental and Numerical Study," *Construction and Building Materials*, **27**, pp. 545–552 (2012).
7. Džiugys, A. and Peters, B., "A New Approach to Detect the Contact of Two-Dimensional Elliptical Particles," *International Journal for Numerical and Analytical Methods in Geomechanics*, **25**, pp. 1487–1500 (2001).
8. Wang, H. and Hao, P., "Numerical Simulation of Indirect Tensile Test Based on the Microstructure of Asphalt Mixture," *Journal of Materials in Civil Engineering*, **23**, pp. 21–29 (2010).
9. Dai, Q., "Prediction of Dynamic Modulus and Phase Angle of Stone-Based Composites Using a Micromechanical Finite-Element Approach," *Journal of Materials in Civil Engineering*, **22**, pp. 618–627 (2009).
10. Masad, E., Muhunthan, B., Shashidhar, N. and Harman, T., "Internal Structure Characterization of Asphalt Concrete Using Image Analysis," *Journal of Computing in Civil Engineering*, **13**, pp. 88–95 (1999).
11. Gatchalian, D., Masad, E., Chowdhury, A. and Little, D., "Characterization of Aggregate Resistance to Degradation in Stone Matrix Asphalt Mixtures," *Transportation Research Record*, pp. 55–63 (2006).
12. Schlangen, E. and Garboczi, E., "Fracture Simulations of Concrete Using Lattice Models: Computational Aspects," *Engineering Fracture Mechanics*, **57**, pp. 319–332 (1997).
13. Ince, R., Arslan, A. and Karihaloo, B., "Lattice Modelling of Size Effect in Concrete Strength," *Engineering Fracture Mechanics*, **70**, pp. 2307–2320 (2003).
14. Yang, S. F., Yang, X. H. and Chen, C. Y., "Simulation of Rheological Behavior of Asphalt Mixture with Lattice Model," *Journal of Central South University of Technology*, **15**, pp. 155–157 (2008).
15. Bazant, Z. P., Tabbara, M. R., Kazemi, M. T. and Pijaudier-Cabot, G., "Random Particle Model for Fracture of Aggregate or Fiber Composites," *Journal of Engineering Mechanics*, **116**, pp. 1686–1705 (1990).
16. Fu, G. and Dekelbab, W., "3D Random Packing of Polydisperse Particles and Concrete Aggregate Grading," *Powder Technology*, **133**, pp. 147–155 (2003).
17. Du, C. B. and Sun, L. G., "Numerical Simulation of Aggregate Shapes of Two-Dimensional Concrete and Its Application," *Journal of Aerospace Engineering*, **20**, pp. 172–178 (2007).
18. Yin, A., Yang, X., Gao, H. and Zhu, H., "Tensile Fracture Simulation of Random Heterogeneous Asphalt Mixture with Cohesive Crack Model," *Engineering Fracture Mechanics*, **92**, pp. 40–55 (2012).
19. Yin, A., Yang, X., Yang, S. and Jiang, W., "Multiscale Fracture Simulation of Three-Point Bending Asphalt Mixture Beam Considering Material Heterogeneity," *Engineering Fracture Mechanics*, **78**, pp.

https://doi.org/10.1017/jmech.2015.36 Published online by Cambridge University Press

2414–2428 (2011).
20. Yin, A., Yang, X., Zeng, G. and Gao, H., "Fracture Simulation of Pre-Cracked Heterogeneous Asphalt Mixture Beam with Movable Three-Point Bending Load," *Construction and Building Materials*, **65**, pp. 232–242 (2014).
21. Zeng, G., Yang, X., Yin, A. and Bai, F., "Simulation of Damage Evolution and Crack Propagation in Three-Point Bending Pre-Cracked Asphalt Mixture Beam," *Construction and Building Materials*, **55**, pp. 323–332 (2014).
22. Collop, A. C., McDowell, G. R. and Lee, Y. W., "Modelling Dilation in an Idealised Asphalt Mixture Using Discrete Element Modelling," *Granular Matter*, **8**, pp. 175–184 (2006).
23. Mo, L., Huurman, M., Wu, S. and Molenaar, A., "2D and 3D Meso-Scale Finite Element Models for Ravelling Analysis of Porous Asphalt Concrete," *Finite Elements in Analysis and Design*, **44**, pp. 186–196 (2008).
24. Xu, R., Yang, X., Yin, A., Yang, S. and Ye, Y., "A Three-Dimensional Aggregate Generation and Packing Algorithm for Modeling Asphalt Mixture with Graded Aggregates," *Journal of Mechanics*, **26**, pp. 165–171 (2010).
25. Yang, S. F., Yang, X. H., Yin, A. Y. and Jiang, W., "Three-Dimensional Numerical Evaluation of Influence Factors of Mechanical Properties of Asphalt Mixture," *Journal of Mechanics*, **28**, pp. 569–578 (2012).
26. Shashidhar, N. and Gopalakrishnan, K., "Evaluating the Aggregate Structure in Hot-Mix Asphalt Using Three-Dimensional Computer Modeling and Particle Packing Simulations," *Canadian Journal of Civil Engineering*, **33**, pp. 945–954 (2006).
27. Coleri, E., Harvey, J. T., Yang, K. and Boone, J. M., "Development of a Micromechanical Finite Element Model from Computed Tomography Images for Shear Modulus Simulation of Asphalt Mixtures," *Construction and Building Materials*, **30**, pp. 783–793 (2012).
28. You, T., Abu Al-Rub, R. K., Darabi, M. K., Masad, E. A. and Little, D. N., "Three-Dimensional Microstructural Modeling of Asphalt Concrete Using a Unified Viscoelastic-Viscoplastic-Viscodamage Model," *Construction and Building Materials*, **28**, pp. 531–548 (2012).
29. Breu, H., Gil, J., Kirkpatrick, D. and Werman, M., "Linear Time Euclidean Distance Transform Algorithms, Pattern Analysis and Machine Intelligence," *IEEE Transactions on Pattern Analysis and Machine Intelligence*, **17**, pp. 529–533 (1995).
30. Vadood, M., Johari, M. S. and Rahaei, A. R., "Introducing a Simple Method to Determine Aggregate Gradation of Hot Mix Asphalt Using Image Processing," *International Journal of Pavement Engineering*, **15**, pp. 142–150 (2013).
31. Fang, Q. and Boas, D. A., "Tetrahedral Mesh Generation from Volumetric Binary and Grayscale Images," *Proceedings of 6th IEEE International Symposium on Biomedical Imaging: From Nano to Macro*, Boston, Massachusetts, U.S.A, pp. 1142–1145 (2009).
32. Kim, Y. R. and Little, D., "Linear Viscoelastic Analysis of Asphalt Mastics," *Journal of Materials in Civil Engineering*, **16**, pp. 122–132 (2004).
33. Park, S. W. and Schapery, R. A., "Methods of Interconversion Between Linear Viscoelastic Material Functions. Part I—A Numerical Method Based on Prony Series," *International Journal of Solids and Structures*, **36**, pp. 1653–1675 (1999).
34. Abbas, A., Papagiannakis, A. and Masad, E., "Linear and Nonlinear Viscoelastic Analysis of the Microstructure of Asphalt Concretes," *Journal of Materials in Civil Engineering*, **16**, pp. 133–139 (2004).

(Manuscript received July 5, 2014,
accepted for publication January 13, 2015.)

https://doi.org/10.1017/jmech.2015.36 Published online by Cambridge University Press